

Optical Control of Polarization Switching in a Single-Component Organic Ferroelectric Crystal

Yuan-Yuan Tang,* Jun-Chao Liu, Yu-Ling Zeng, Hang Peng, Xue-Qin Huang, Meng-Juan Yang, and Ren-Gen Xiong*



Cite This: *J. Am. Chem. Soc.* 2021, 143, 13816–13823



Read Online

ACCESS |



Metrics & More

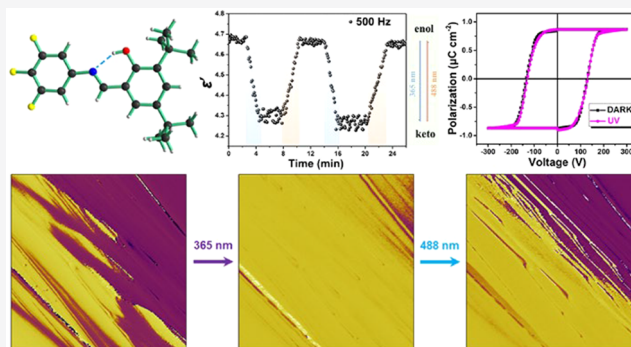


Article Recommendations



Supporting Information

ABSTRACT: The optical control of polarization switching is attracting tremendous interest because photoirradiation stands out as a nondestructive, noncontact, and remote-control means beyond an electric or strain field. The current research mainly uses various photoexcited electronic effects to achieve the photocontrol polarization, such as a light-driven flexoelectric effect and a photovoltaic effect. However, since photochromism was discovered in 1867, the structural phase transition caused by photoisomerization has never been associated with ferroelectricity. Here, we successfully synthesized an organic photochromic ferroelectric with polar space group *Pna*2₁, 3,4,5-trifluoro-*N*-(3,5-di-*tert*-butylsalicylidene)aniline, whose color can change between yellow and orange via laser illumination. Its dielectric permittivity and spontaneous polarization can be switched reversibly with a photoinduced phase transition triggered by structural photoisomerization between the enol form and the *trans*-keto form. To our knowledge, this is the first photoswitchable ferroelectric crystal to achieve polarization switching through a structural phase transition triggered by photoisomerization. This finding paves the way toward photocontrol of smart materials and biomechanical applications in the future.



INTRODUCTION

Ferroelectricity, identified by switchable spontaneous polarization (P_s), has revolutionized important technologies such as memory elements and continues to generate novel functional materials and intriguing phenomena.^{1–3} Since Valasek discovered ferroelectricity in Rochelle salt in 1920, ferroelectric materials have been used extensively in many fields, such as surface acoustic wave devices, electro-optic photonic devices, pyroelectric infrared detectors, medical ultrasound equipment, and nonvolatile memories.^{4–9} A ferroelectric is usually a thermodynamic structural phase transition material, which can undergo a reversible paraelectric–ferroelectric phase transition in response to temperature, resulting in the appearance and disappearance of spontaneous polarization.^{10–19} Such structural phase transitions induced by temperature have been well studied, and there are also many ferroelectrics that can exhibit structural transitions when they are subjected to changes in pressure, composition, and magnetic field.^{20–25} As a non-destructive, noncontact, and remotely induced medium, light has long been a coveted manipulation tool. However, until now, no ferroelectric materials have been found to undergo a photoinduced structural phase transition that can cause polarization switching.

At present, the research on the optical control of polarization switching has basically focused on inorganic ferroelectrics.^{26–31}

They mainly rely on various photoexcited electronic effects to realize the photocontrol polarization, such as a light-driven flexoelectric effect and the mediation of a photovoltaic effect.^{26–31} For example, the rapid formation of surface strain and subsequent flexoelectricity achieved by photoirradiation can induce lattice vibrations and eventually metastable ferroelectricity in the quantum paraelectric SrTiO₃.³² However, intrinsic ferroelectric properties resulting from structural phase transitions directly driven by light have never been reported. It is noted that there is a class of important organic materials that can display photochromism in the crystalline state, represented by Schiff bases of salicylaldehyde with amines.^{33–37} Photochromism originates from photoinduced geometrical isomerization such as *trans*–*cis* or enol–keto isomerization, which can trigger a type of photoinduced structural phase transition different from a thermodynamic transition.^{38,39} Under the necessary condition of ensuring that compounds crystallize in one of the 10 polar point groups,¹ these types of materials could be regarded as

Received: June 13, 2021

Published: August 23, 2021



kinds of photoswitchable ferroelectrics, whose polarization would be expectedly switched by the reversible structural photoisomerizations.

In this work, we successfully synthesized a single-component organic compound, 3,4,5-trifluoro-*N*-(3,5-di-*tert*-butylsalicylidene)aniline (TFTBSA), which can crystallize in the polar space group $Pna2_1$ (TFTBSA-1) and the centrosymmetric nonpolar space group $P2_1/n$ (TFTBSA-2) under various crystal growth conditions (Table S1 and Figure S1). Upon ultraviolet (UV) light irradiation of 365 nm, the color of TFTBSA-1 crystals can change from yellow to orange (Figure 1), while that of TFTBSA-2 crystals stays almost the same

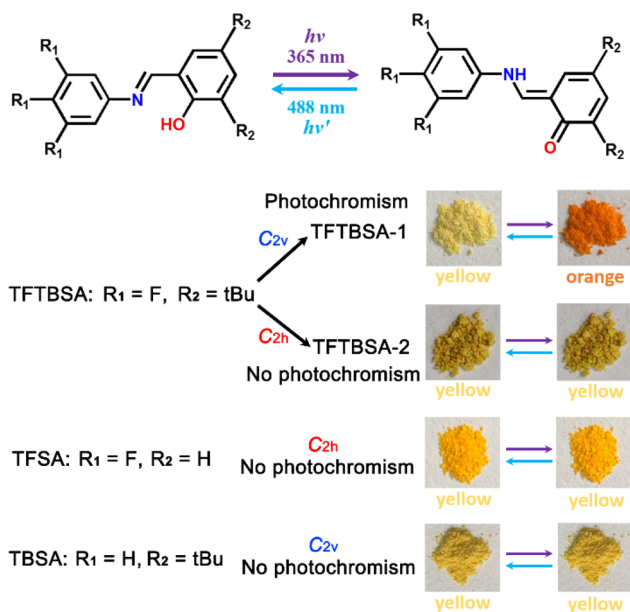


Figure 1. Chemical structures and physical properties of TFTBSA, TFSA, and TBSA (tBu = *tert*-butyl). Enol–keto photoisomerization exists in TFTBSA-1. The enol form is converted into the *trans*-keto form by UV light irradiation of 365 nm. The *trans*-keto form returns to the enol form upon visible light irradiation or light irradiation of 488 nm.

(Figure 1 and Figure S2). Solid-state ultraviolet–visible (UV–vis) absorption and infrared (IR) spectra confirm that TFTBSA-1 undergoes a photoinduced phase transition accompanied by a reversible structural photoisomerization between the enol form and the *trans*-keto form, which is impossible to be realized in inorganic ferroelectrics. Under the remote-control photoirradiation, the dielectric permittivity and spontaneous polarization can be switched reversibly by structural photoisomerization. To the best of our knowledge, this is the first photoswitchable ferroelectric to achieve polarization switching through a structural phase transition triggered by photoisomerization. These attributes hold promise for on-chip optical interconnects and optoelectronic logic-in-memory devices^{40,41} and will bring revolutionary changes to the photocontrol of smart materials and biomechanical applications in the future.

RESULTS AND DISCUSSION

We also synthesized two single-component organic compounds, 3,4,5-trifluoro-*N*-(salicylidene)aniline (TFSA) and *N*-(3,5-di-*tert*-butylsalicylidene)aniline (TBSA). TFSA crystallizes in the same centrosymmetric nonpolar space group $P2_1/n$ as that of TFTBSA-2, which does not meet the necessary conditions for

becoming a ferroelectric that crystals must crystallize in one of the 10 polar point groups, 1 (C_1), 2 (C_2), m (C_s), $mm2$ (C_{2v}), 4 (C_4), $4mm$ (C_{4v}), 3 (C_3), $3m$ (C_{3v}), 6 (C_6), and $6mm$ (C_{6v}) (Table S1, Figure 1, and Figure S3). Hence, both TFSA and TFTBSA-2 can not obtain ferroelectricity at room temperature. Although TBSA crystallizes in the same polar space group $Pna2_1$ as that of TFTBSA-1, which has been reported previously by Uddin Ahmad et al.,⁴² it does not undergo either a thermodynamic structural phase transition or a photoinduced transition (Table S1, Figure 1, and Figure S4). We thus failed to observe ferroelectric domains and polarization switching before or after UV light illumination of 365 nm. Consequently, it is necessary for a compound to crystallize in a polar point group and have photoisomerization at the same time to achieve photocontrolled polarization switching.

A crystal structure determination reveals the TFTBSA-1 adopts the enol form with the C=N double bond in the *trans* configuration at room temperature, stabilized by an intramolecular O–H...N hydrogen bond (Figure S5). The light-driven phase transition might be induced by the molecular photoisomerization from the enol form to the *trans*-keto form (Figure 1). However, because the conversion ratio of this photoisomerization is insufficient for an X-ray structure determination, the detected structure is still composed of almost all enol molecules, and the pure *trans*-keto molecules cannot be isolated, giving almost the same cell parameters in the crystal structures before and after UV light illumination of 365 nm (Table S2). Fortunately, the *trans*-keto molecules can be determined by other measurements and calculations (Figure 2).

We first calculated the HOMO (highest occupied molecular orbital) and LUMO (lowest unoccupied molecular orbital) of

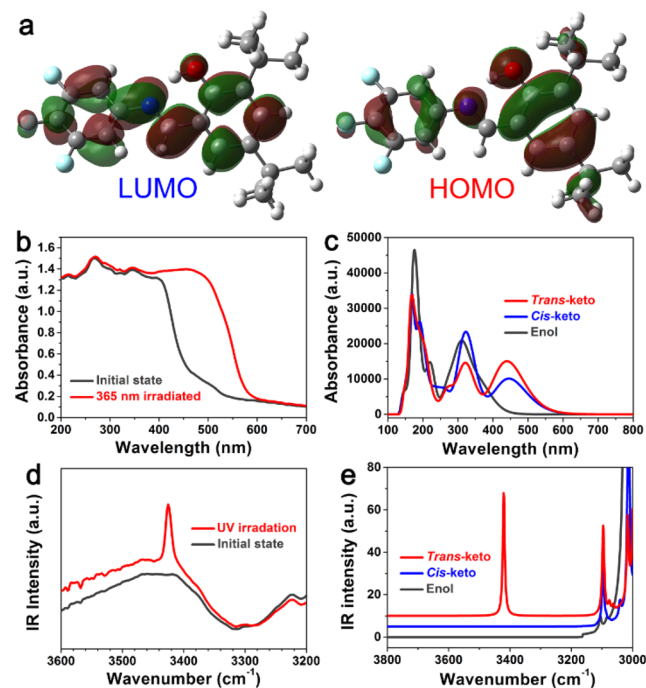


Figure 2. (a) HOMO and LUMO of the TFTBSA-1 molecule. (b) Experimental UV–vis spectra of TFTBSA-1 under ambient conditions and after UV irradiation. (c) Calculated UV–vis spectra of TFTBSA-1 with enol, *cis*-keto and *trans*-keto forms, respectively. (d) Experimental IR absorption spectra of TFTBSA-1 under ambient conditions and after UV irradiation. (e) Calculated IR absorption spectra of the TFTBSA-1 series with enol, *cis*-keto, and *trans*-keto forms, respectively.

the TFTBSA-1 molecule to get a deep insight into its electronic structure (Figure 2a). From the HOMO of the TFTBSA-1 molecule, the electron density is mainly distributed on the benzene ring from the salicylaldehyde part. In comparison with the HOMO, the LUMO has a significant shift to the C–N direction. The resultant energy gap between HOMO and LUMO is 0.14296 hartree, corresponding to an energy of 3.89 eV, which corresponds to absorption at a wavelength of 319 nm.

Solid state UV–vis absorption spectra were recorded before and after UV irradiation to investigate the variation of the color change (Figure 2b). Under ambient conditions, TFTBSA-1 crystals absorb light of less than 450 nm, in good accordance with their yellow appearance. However, under UV irradiation, a new absorption band emerges from 450 to 580 nm, which is consistent with the orange color. Therefore, the photochromic effect should be attributed to the appearance of new absorption bands after UV irradiation. In addition, the calculated UV–vis spectra of molecular configuration of enol and *cis*- and *trans*-keto forms reflect obvious differences (Figure 2c). The absorption peak centered at a wavelength of 311 nm in the enol form is close to the 319 nm estimated by the HOMO and LUMO. In comparison with the enol form, the *cis*- or *trans*-keto form displays new absorption bands at long wavelengths (400–550 nm). This huge signal change originates from the great conformational change of the molecule after UV illumination, which leads to a corresponding change in the electronic transition of TFTBSA-1 molecules.

We also examined the time-related solid state UV–vis absorption spectra of TFTBSA-1 to monitor the photoreaction process. As shown in Figure S6a, a new absorption band emerges from 450 to 580 nm and reaches saturation within 20 s under UV irradiation ($\lambda = 365$ nm), indicating the completion of the photoreaction equilibrium from the enol form to the keto form under this condition. Under visible light irradiation of 488 nm, the keto photoproduct quickly recovers to the initial enol form within 8 s (Figure S6b). The photoreaction rate of TFTBSA-1 obviously decreased rapidly with an increase of illumination time, indicating that most of the enol–keto phototransformation was completed during the initial 3–5 s (Figure S7). Moreover, we obtained the spectra of both a TFTBSA-1 film and a polycrystalline sample before and after UV irradiation to estimate the reaction yield (Figure 2b and Figure S8). First, we assume that, in the initial state, the UV–vis absorption spectrum has no absorption at 450–580 nm, which corresponds to a enol–keto conversion rate of 0%; when the photoreaction yield reaches 100%, the absorption peak of the *trans*-keto form photoproduct at 450–580 nm will be the highest value from 200 to 800 nm.^{43,44} On the basis of this assumption, after the spectral data are normalized, it can be roughly inferred that the conversion rates of powder samples and film samples are at most about 88% and 37%, respectively (Table S3). The high conversion ratio of powder samples is because the diffuse reflection mode basically measures the UV–vis absorption spectrum of the sample surface. Although the conversion ratio from the enol form to the *trans*-keto form is not high for the crystals, the photoisomerization of the sample surface should be basically complete.

To explore the origin of changes in molecular conformation before and after UV illumination, we measured and calculated the infrared (IR) spectra of TFTBSA-1. The most obvious change in IR spectra is that a new absorption peak centered at 3425 cm^{-1} appears after UV irradiation (Figure 2d). According to the experimentally measured single-crystal X-ray diffraction

structure, we constructed several different molecular conformations: enol, *cis*-keto, and *trans*-keto forms (Figures S9–S11). Further frequency calculations reflect that only the *trans*-keto form displays a peak at a range greater than 3100 cm^{-1} (Figure 2e). The calculated wavenumber (3420 cm^{-1}) is attributed to the free N–H stretching vibration, which is close to the measured IR absorption peak. Due to the formation of an N–H...O hydrogen bond, the *cis*-keto form has no free N–H stretching vibration mode. Therefore, the most likely change of the molecule is the change from the enol form to the *trans*-keto form. We thus calculated the dipole moment of enol and *trans*-keto configurations before and after light irradiation (Figure 3a).

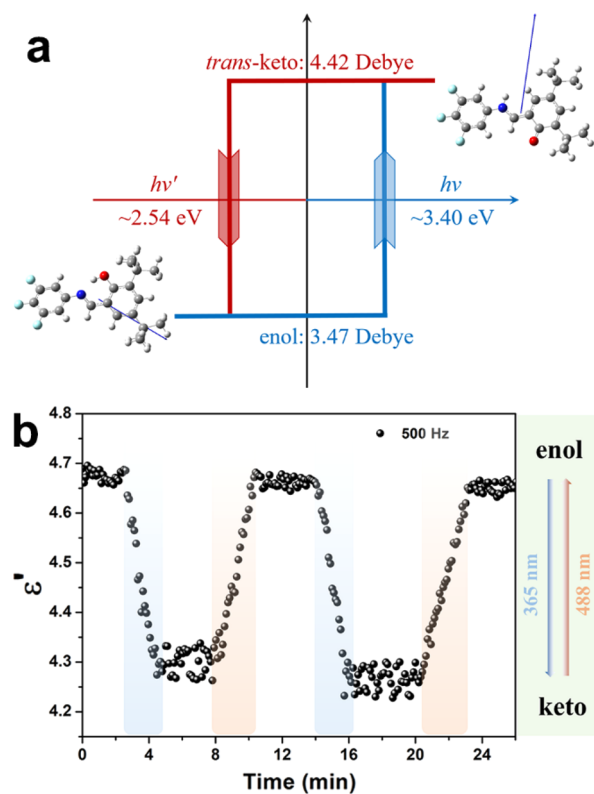


Figure 3. (a) Schematic diagram of the molecular conformation transformation of TFTBSA-1. The blue arrow in the molecule indicates the direction of the molecular dipole. (b) The real part of the complex dielectric constant of TFTBSA-1 at room temperature: the initial state, the state after UV illumination of 365 nm, and then the state after visible illumination of 488 nm.

Under ambient conditions, TFTBSA-1 molecules adopt the enol form with 3.47 D. After light illumination of 365 nm, the molecular dipole moment increased to 4.42 D as the molecule transformed to the *trans*-keto form. Further illumination with 488 nm light can transfer the *trans*-keto form back to the enol form.

A differential scanning calorimetry (DSC) analysis reflects that there is no phase transition before the melting point of 375.6 K in TFTBSA-1 (Figure S12a). Moreover, the real part (ϵ') of the complex dielectric constant of TFTBSA-1 remains the same and shows no obvious anomalies at different frequencies in the heating run, further proving that no thermal phase transition exists (Figure S12b). The above results have shown that TFTBSA-1 undergoes an enol–keto transition after UV illumination; thus, the dielectric permittivities of the two forms should also be different. As shown in Figure 3b, the real part ϵ' of

the dielectric constant at 500 Hz remains at about 4.65–4.70 in the enol form and exhibits a slow drop to 4.25–4.30 with the approach of UV light irradiation of 365 nm for about 2 min, corresponding to the *trans*-keto form. After visible light irradiation of 488 nm for about 3 min, the real part ϵ' can gradually return to its original state. Therefore, the enol–keto transition under UV and visible illumination results in a dielectric switching between the high-dielectric state (the enol form) and the low-dielectric state (the *trans*-keto form).

The second-harmonic generation (SHG) signal was obtained to detect the crystal symmetry of TFTBSA, where TFTBSA-1 displays an active SHG signal with an intensity about one-fifth of that of KH_2PO_4 (KDP) at room temperature, corresponding well to the polar point group $mm2$ (C_{2v}) in the structure (Figures S4 and S13a), while a noise-level signal was observed in TFTBSA-2, agreeing well with the centrosymmetric point group $2/m$ (C_{2h}) (Figure S13b). Ferroelectricity might be realized in the crystals that adopt a polar point group, such as the polar $mm2$ (C_{2v}) point group for TFTBSA-1. To confirm this, we carried out polarization–electric field (P – E) hysteresis loop measurements for TFTBSA-1. Using the double-wave method,⁴⁵ we observed a well-shaped P – E ferroelectric hysteresis loop for the TFTBSA-1 thin film at room temperature in the dark, providing solid proof for ferroelectricity in TFTBSA-1 (Figure 4). The measured

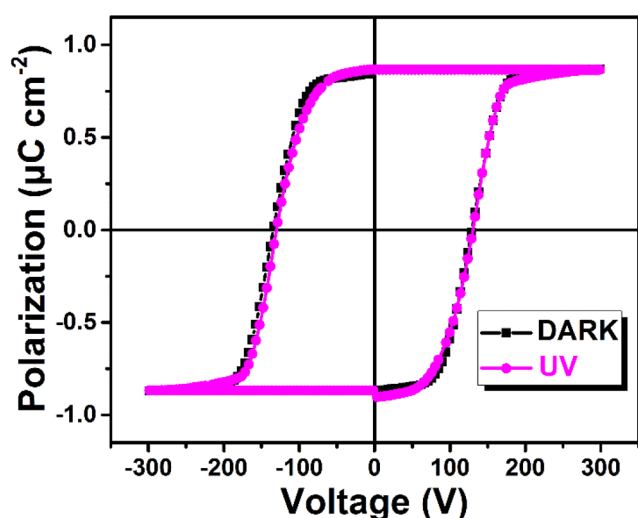


Figure 4. P – E hysteresis loops of the TFTBSA-1 thin film via a double-wave method at room temperature under dark conditions and after UV illumination of 365 nm.

spontaneous polarization P_s of TFTBSA-1 obtained from the hysteresis loop is about $0.87 \mu\text{C cm}^{-2}$, close to that of the recently discovered two-dimensional and three-dimensional lead halide perovskite ferroelectrics [4,4-difluorohexahydroazepine]₂PbI₄ ($1.1 \mu\text{C cm}^{-2}$) and [2-trimethylammonioethylammonium]Pb₂Cl₆ ($1.0 \mu\text{C cm}^{-2}$) and larger than that of Rochelle salt ($0.25 \mu\text{C cm}^{-2}$).^{46–48} The coercive electric voltage is about 132 V for an $\sim 33.8 \mu\text{m}$ thick film, corresponding to a coercive field of 39.1 kV/cm. Upon UV light irradiation of 365 nm, the P – E hysteresis loop does not change significantly, probably because the conversion ratio of photoisomerization is not high.

In order to estimate the ferroelectric polarization of the crystal, we first calculated the vector sum of the dipole moments of the molecules in the unit cell. As shown in Figure S9, the dipole moment of TFTBSA-1 is 3.47 D. Taking into account the

arrangement and dipole orientation of the molecules in the unit cell, we estimate the total polarization value to be about $1.26 \mu\text{C cm}^{-2}$. Furthermore, we employed the Berry phase method to gain a more accurate value of ferroelectric polarization, from which polarization with $1.85 \mu\text{C cm}^{-2}$ along the c axis can be extracted. However, the polarization along the a and b axes is zero, which is in good accordance with the symmetry requirement of space group $Pna2_1$. The difference in the computed polarizations between the vector sum of the dipole moments and the Berry phase method can be attributed to the neglected intermolecular interactions and stacking effects from the former.

To further prove the ferroelectricity of TFTBSA-1, two effects have to be demonstrated: the existence of domains with different orientations of polarization and hysteretic switching between the opposite domain states by electric fields. The piezoresponse force microscopy (PFM) technique enables the visualization and control of ferroelectric domains, as well as direct measurements of the local ferroelectric hysteresis loop.^{49–51} Hence, we performed PFM measurements to investigate the ferroelectric behavior of TFTBSA-1. Figure 5a,b shows the PFM images taken after electrical poling over the central region with a tip voltage of +100 V, which present a long-lasting bistable domain pattern separated by a clear domain wall. Further, a box-in-box domain pattern was written via the application of a tip voltage of -80 V over the center region of the newly generated yellow domain (Figure 5c,d). During the poling processes, the surface morphology of the TFTBSA-1 thin film displays no obvious damage (Figure 5e). These results suggest that the polarization in TFTBSA-1 is switchable.

In addition, PFM switching spectroscopy was used to measure the corresponding hysteresis loops. Figure 5f–h shows the PFM amplitude and phase loops for TFTBSA-1 at the initial state, after UV light illumination of 365 nm, and after visible light illumination of 488 nm, respectively. The butterfly-shaped amplitude loops and hysteresis phase loops confirmed the ferroelectric switching for TFTBSA-1 under these three states.

Next, the optical control of the domains in TFTBSA-1 was investigated in the thin film samples as well. The out-of-plane PFM phase image of the initial domain pattern captured in the dark is shown in Figure 6a. Figure 6b displays the postoptical poling domain structure, which was acquired immediately upon UV light irradiation of 365 nm, showing that the purple domains have become smaller. Then, the purple domains can be entirely switched to yellow domains after 70 min of continuous laser exposure of 365 nm (Figure 6c). Subsequently, part of the yellow domains recovered to the purple domains after visible light irradiation of 488 nm (Figure 6d). Detailed topography and PFM amplitude information is given in Figure S14. During the laser exposure, the morphology of the sample does not change and the domain walls can be discerned in the corresponding amplitude images, excluding the artifact imaging. Hence, in this region, the 365 nm laser illumination favors the formation of yellow domains, while the 488 nm laser illumination favors the formation of purple domains.

To exclude the influence of photothermal effect on the domain structure, and to demonstrate the repeatability of the process, we subjected another region with poly domains to heat treatment and laser illumination in turn (Figure S15). The results ruled out the effect of temperature changes due to laser exposure and confirmed the repeatability of the optical control of the domains in TFTBSA-1. Consequently, the photoisomerization of TFTBSA-1 should be responsible for the

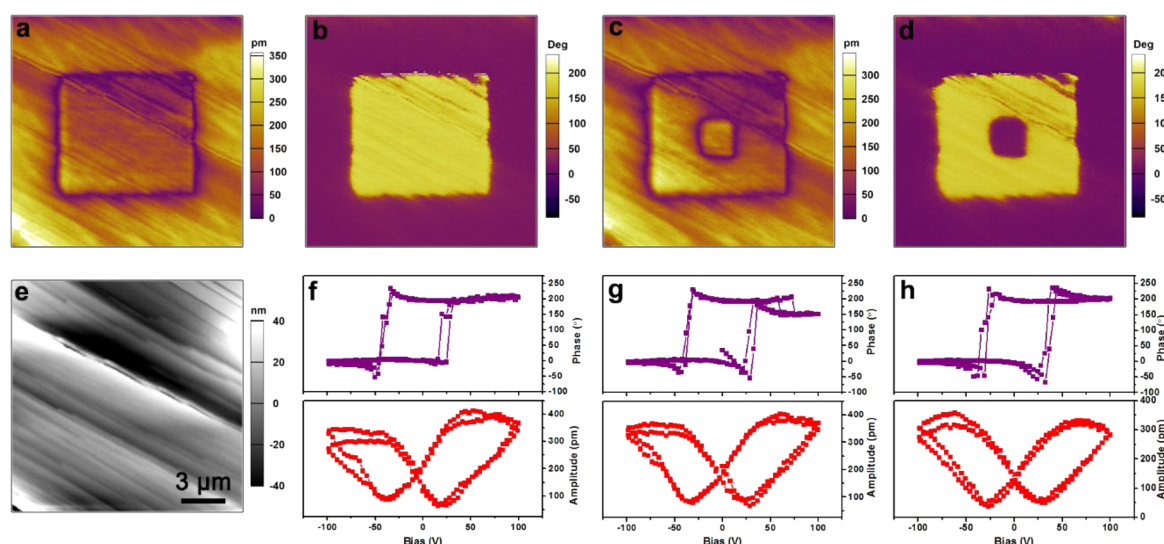


Figure 5. Electric field induced polarization switching in a TFTBSA-1 thin film. (a) PFM amplitude and (b) phase images after writing the central region with a +100 V tip voltage. (c) PFM amplitude and (d) phase images after a second electric writing with a -80 V tip voltage. (e) Topographic image acquired after electric writing. The surface roughness is 14.626 nm for the film morphology. (f–h) PFM switching spectroscopy measurements for the thin film under dark conditions (f), under UV light irradiation of 365 nm (g) and under visible light irradiation of 488 nm (h), respectively.

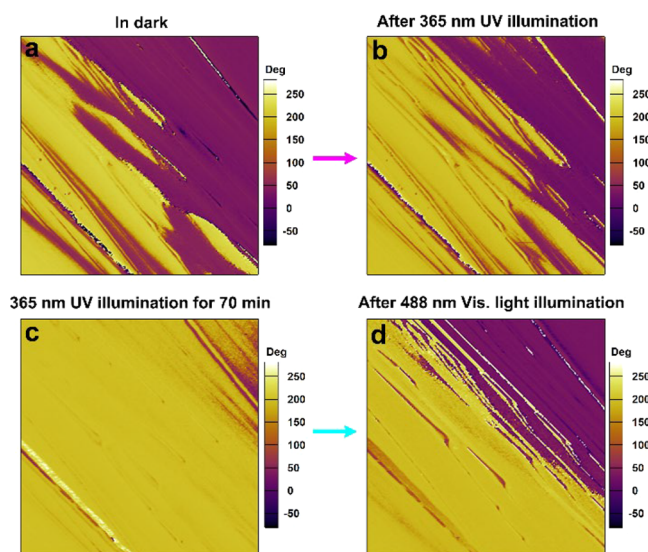


Figure 6. Light-induced manipulation of domains in a TFTBSA-1 thin film: out-of-plane PFM phase images for (a) acquisition of the initial domain pattern under dark conditions, (b) immediate acquisition after UV light irradiation of 365 nm, (c) acquisition after 70 min of continuous laser exposure of 365 nm, (d) acquisition after visible light irradiation of 488 nm.

observed domain evolution under different laser illuminations. The transformation between the enol and the *trans*-keto form under laser exposure can change the polarization in TFTBSA-1 and thus change the domains.

In order to reveal the possible mechanism of ferroelectric polarization switching, we therefore conducted a systematic analysis of the crystal structure of TFTBSA-1. As shown in Figure 7a, TFTBSA-1 molecules align along the *a* axis in a head-to-tail manner. C–O and C–N bonds in TFTBSA-1 molecules both point to the same side, thereby generating spontaneous polarization along the *c* axis. Significantly, the adjacent TFTBSA-1 molecules are stacked in the form of dislocation in the *ab* plane, and the distance between the upper and lower

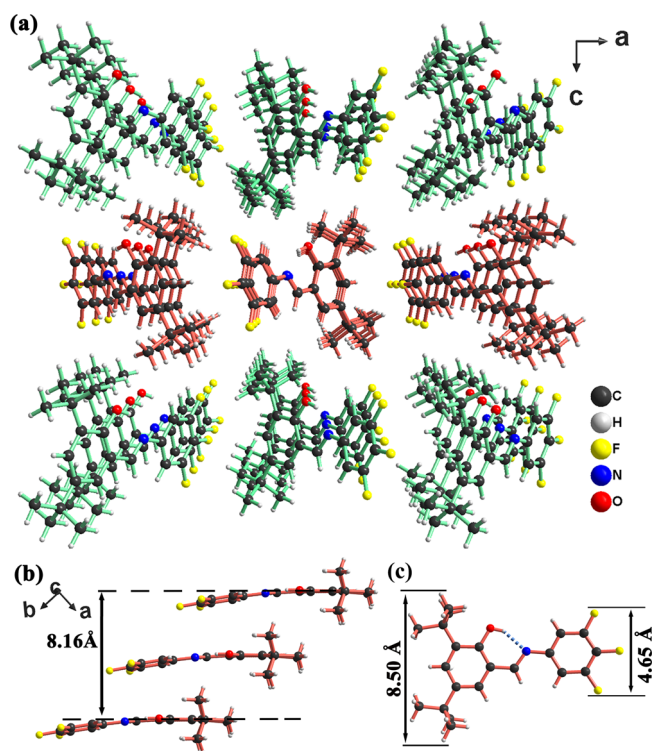


Figure 7. (a) Packing diagram of TFTBSA-1 at 293 K along the *b* axis. (b) Packing diagram of TFTBSA-1 at 293 K in the *ab* plane. (c) Molecular structure of TFTBSA-1, showing its longitudinal length.

TFTBSA-1 molecules is about 8.16 Å, which leaves enough space for the flipping movement of TFTBSA-1 molecules, considering their maximum width of 8.50 Å in the dislocation and 4.65 Å at the overlap (Figure 7b,c). For a better understanding of the 180° flip motion of the π -planar molecule driven by the electric field, we constructed bistable state atomic structure models with opposite polarizations (Figure S16). The superposition of two ferroelectric states with opposite polarizations forms a reference phase in which the polarization

completely cancels out (Figure S16b). This reference phase with zero polarization resembles a configuration with dual orientation disorder. A similar 180° flip motion of the π -planar molecule exists in the supramolecular rotator ferroelectric (*m*-fluoroanilinium)(dibenzo[18]crown-6)[Ni(dmit)₂] (dmit²⁻ = 2-thioxo-1,3-dithiole-4,5-dithiolate).⁵²

The photochromic mechanism of TFTBSA-1 should be similar to that of other salicylidene aniline derivatives, which involves the transfer of a proton from the phenolic OH group of the enol form to the N atom of the imine group, generating the *cis*-keto form that is subsequently converted into the *trans*-keto form.^{53,54} The transformation from the *cis*-keto form to the *trans*-keto form might occur via a pedal motion in a manner similar to the thermal motion of azobenzene crystals.⁵⁵ In comparison to TBSA, three F atoms on the aniline ring of TFTBSA-1 have superelectronnegativity, which makes the electron cloud on the benzene ring and the lone pair on the imine N atom deviate to the side of F atoms and finally weakens the O–H...N hydrogen bonding interaction (Figure S17). With the weakening of the hydrogen-bonding interaction, the energy barrier for the enol–keto transition of TFTBSA-1 is lower than that of TBSA, which makes it occur more easily.³³ Moreover, as shown in Figure 7a and Figure S18a, TBSA shows an X-shaped cross arrangement in the *ac* plane, while TFTBSA-1 is in a parallel arrangement, which makes TBSA more compact in stacking. Meanwhile, there are weak interactions between adjacent TBSA molecules, which greatly hinder the progress of its photochromic reaction (Figure S18b). Hence, the synergistic effect of molecular arrangements and the intra- and intermolecular interactions causes difficulty for TBSA to produce photochromic behavior.

CONCLUSION

In summary, we present the reversible optical control of polarization switching in a photoswitchable organic ferroelectric crystal. Such a photoinduced polarization switching is caused by a reversible photoresponsive structural phase transition with enol–keto photoisomerization. It can be achieved by simple photoirradiation without resorting to specific conditions. This finding provides a new mechanism and material system for optically controlled ferroelectric polarization switching, which holds promise for a new generation of optical ferroelectric devices. It is foreseeable that more photoswitchable ferroelectric crystals will be developed, which are expected to be capable of competing with polarization switching achieved by applying an electric or strain field.

ASSOCIATED CONTENT

Supporting Information

The Supporting Information is available free of charge at <https://pubs.acs.org/doi/10.1021/jacs.1c06108>

Experimental details and characterization methods, additional crystal structures, PFM images, and UV–vis spectra, molecular structure, DSC curve, SHG measurements, PXRD patterns, crystal photograph, thermogravimetric analysis, and crystal data and structure information (PDF)

Color change of TBSA crystals under UV illumination of 365 nm (MP4)

Accession Codes

CCDC 2089633–2089636, 2089638–2089639, and 2089642 contain the supplementary crystallographic data for this paper.

These data can be obtained free of charge via www.ccdc.cam.ac.uk/data_request/cif, or by emailing data_request@ccdc.cam.ac.uk, or by contacting The Cambridge Crystallographic Data Centre, 12 Union Road, Cambridge CB2 1EZ, UK; fax: +44 1223 336033.

AUTHOR INFORMATION

Corresponding Authors

Yuan-Yuan Tang — Ordered Matter Science Research Center, Nanchang University, Nanchang 330031, People's Republic of China; orcid.org/0000-0002-8369-572X; Email: tangyuan@ncu.edu.cn

Ren-Gen Xiong — Ordered Matter Science Research Center, Nanchang University, Nanchang 330031, People's Republic of China; orcid.org/0000-0003-2364-0193; Email: xiongrg@seu.edu.cn

Authors

Jun-Chao Liu — Ordered Matter Science Research Center, Nanchang University, Nanchang 330031, People's Republic of China

Yu-Ling Zeng — Ordered Matter Science Research Center, Nanchang University, Nanchang 330031, People's Republic of China

Hang Peng — Ordered Matter Science Research Center, Nanchang University, Nanchang 330031, People's Republic of China

Xue-Qin Huang — Ordered Matter Science Research Center, Nanchang University, Nanchang 330031, People's Republic of China

Meng-Juan Yang — Ordered Matter Science Research Center, Nanchang University, Nanchang 330031, People's Republic of China

Complete contact information is available at: <https://pubs.acs.org/10.1021/jacs.1c06108>

Notes

The authors declare no competing financial interest.

ACKNOWLEDGMENTS

The manuscript was improved by insightful reviews by the anonymous reviewers. This work was supported by the National Natural Science Foundation of China (21991142, 21831004, 21975114 and 11904151).

REFERENCES

- (1) Lines, M. E.; Glass, A. M. *Principles and applications of ferroelectrics and related materials*; Oxford University Press: 2001; pp 1–672.
- (2) Scott, J. F. Applications of modern ferroelectrics. *Science* **2007**, *315*, 954–959.
- (3) Eerenstein, W.; Mathur, N. D.; Scott, J. F. Multiferroic and magnetoelectric materials. *Nature* **2006**, *442*, 759–765.
- (4) Valasek, J. Piezo-electric and allied phenomena in Rochelle salt. *Phys. Rev.* **1921**, *17*, 475.
- (5) Li, W.; Wang, Z.; Deschler, F.; Gao, S.; Friend, R. H.; Cheetham, A. K. Chemically diverse and multifunctional hybrid organic–inorganic perovskites. *Nat. Rev. Mater.* **2017**, *2*, 16099.
- (6) Xu, W.-J.; Kopyl, S.; Kholkin, A.; Rocha, J. Hybrid organic–inorganic perovskites: Polar properties and applications. *Coord. Chem. Rev.* **2019**, *387*, 398–414.
- (7) Long, J.; Ivanov, M. S.; Khomchenko, V. A.; Mamontova, E.; Thibaud, J.-M.; Rouquette, J.; Beaudhuin, M.; Granier, D.; Ferreira, R. A. S.; Carlos, L. D.; Donnadieu, B.; Henriques, M. S. C.; Paixão, J. A.; Guari, Y.; Larionova, J. Room temperature magnetoelectric coupling in

- a molecular ferroelectric ytterbium(III) complex. *Science* **2020**, *367*, 671–676.
- (8) Zhang, H.-Y.; Tang, Y.-Y.; Shi, P.-P.; Xiong, R.-G. Toward the Targeted Design of Molecular Ferroelectrics: Modifying Molecular Symmetries and Homochirality. *Acc. Chem. Res.* **2019**, *52*, 1928–1938.
- (9) Liu, H.-Y.; Zhang, H.-Y.; Chen, X.-G.; Xiong, R.-G. Molecular Design Principles for Ferroelectrics: Ferroelectrochemistry. *J. Am. Chem. Soc.* **2020**, *142*, 15205–15218.
- (10) Morita, H.; Tsunashima, R.; Nishihara, S.; Inoue, K.; Omura, Y.; Suzuki, Y.; Kawamata, J.; Hoshino, N.; Akutagawa, T. Ferroelectric Behavior of a Hexamethylenetetramine-Based Molecular Perovskite Structure. *Angew. Chem., Int. Ed.* **2019**, *58*, 9184–9187.
- (11) Anetai, H.; Takeda, T.; Hoshino, N.; Kobayashi, H.; Saito, N.; Shigeno, M.; Yamaguchi, M.; Akutagawa, T. Ferroelectric Alkylamide-Substituted Helicene Derivative with Two-Dimensional Hydrogen-Bonding Lamellar Phase. *J. Am. Chem. Soc.* **2019**, *141*, 2391–2397.
- (12) Xu, G. C.; Zhang, W.; Ma, X. M.; Chen, Y. H.; Zhang, L.; Cai, H. L.; Wang, Z. M.; Xiong, R. G.; Gao, S. Coexistence of magnetic and electric orderings in the metal-formate frameworks of $[\text{NH}_4][\text{M}(\text{HCOO})_3]$. *J. Am. Chem. Soc.* **2011**, *133*, 14948–14951.
- (13) Harada, J.; Shimojo, T.; Oyamaguchi, H.; Hasegawa, H.; Takahashi, Y.; Satomi, K.; Suzuki, Y.; Kawamata, J.; Inabe, T. Directionally tunable and mechanically deformable ferroelectric crystals from rotating polar globular ionic molecules. *Nat. Chem.* **2016**, *8*, 946–952.
- (14) Xu, W.-J.; Romanyuk, K.; Martinho, J. M. G.; Zeng, Y.; Zhang, X.-W.; Ushakov, A.; Shur, V.; Zhang, W.-X.; Chen, X.-M.; Kholkin, A.; Rocha, J. Photoresponsive Organic–Inorganic Hybrid Ferroelectric Designed at the Molecular Level. *J. Am. Chem. Soc.* **2020**, *142*, 16990–16998.
- (15) Liu, Y.; Han, S.; Wang, J.; Ma, Y.; Guo, W.; Huang, X.-Y.; Luo, J.-H.; Hong, M.; Sun, Z. Spacer Cation Alloying of a Homoconformational Carboxylate trans Isomer to Boost in-Plane Ferroelectricity in a 2D Hybrid Perovskite. *J. Am. Chem. Soc.* **2021**, *143*, 2130–2137.
- (16) Li, L.; Liu, X.; He, C.; Wang, S.; Ji, C.; Zhang, X.; Sun, Z.; Zhao, S.; Hong, M.; Luo, J. A Potential Sn-Based Hybrid Perovskite Ferroelectric Semiconductor. *J. Am. Chem. Soc.* **2020**, *142*, 1159–1163.
- (17) Li, D.; Zhao, X.-M.; Zhao, H.-X.; Dong, X.-W.; Long, L.-S.; Zheng, L.-S. Construction of Magnetolectric Composites with a Large Room-Temperature Magnetolectric Response through Molecular–Ionic Ferroelectrics. *Adv. Mater.* **2018**, *30*, 1803716.
- (18) Katrusiak, A.; Szafranski, M. Ferroelectricity in $\text{NH}\cdots\text{N}$ hydrogen bonded crystals. *Phys. Rev. Lett.* **1999**, *82*, 576.
- (19) Shi, C.; Ye, L.; Gong, Z.-X.; Ma, J.-J.; Wang, Q.-W.; Jiang, J.-Y.; Hua, M.-M.; Wang, C.-F.; Yu, H.; Zhang, Y.; Ye, H.-Y. Two-Dimensional Organic–Inorganic Hybrid Rare-Earth Double Perovskite Ferroelectrics. *J. Am. Chem. Soc.* **2020**, *142*, 545–551.
- (20) Tang, Y.-Y.; Li, P.-F.; Liao, W.-Q.; Shi, P.-P.; You, Y.-M.; Xiong, R.-G. Multiaxial Molecular Ferroelectric Thin Films Bring Light to Practical Applications. *J. Am. Chem. Soc.* **2018**, *140*, 8051–8059.
- (21) Ai, Y.; Zeng, Y.-L.; He, W.-H.; Huang, X.-Q.; Tang, Y.-Y. Six-Fold Vertices in a Single-Component Organic Ferroelectric with Most Equivalent Polarization Directions. *J. Am. Chem. Soc.* **2020**, *142*, 13989–13995.
- (22) Besara, T.; Jain, P.; Dalal, N. S.; Kuhns, P. L.; Reyes, A. P.; Kroto, H. W.; Cheetham, A. K. Mechanism of the order-disorder phase transition, and glassy behavior in the metal-organic framework $[(\text{CH}_3)_2\text{NH}_2]\text{Zn}(\text{HCOO})_3$. *Proc. Natl. Acad. Sci. U. S. A.* **2011**, *108*, 6828–6832.
- (23) Asamitsu, A.; Moritomo, Y.; Tomioka, Y.; Arima, T.; Tokura, Y. A structural phase transition induced by an external magnetic field. *Nature* **1995**, *373*, 407–409.
- (24) Kuwahara, H.; Tomioka, Y.; Asamitsu, A.; Moritomo, Y.; Tokura, Y. A First-Order Phase Transition Induced by a Magnetic Field. *Science* **1995**, *270*, 961–963.
- (25) Shi, P.-P.; Tang, Y.-Y.; Li, P.-F.; Liao, W.-Q.; Wang, Z.-X.; Ye, Q.; Xiong, R.-G. Symmetry breaking in molecular ferroelectrics. *Chem. Soc. Rev.* **2016**, *45*, 3811–3827.
- (26) Kreisel, J.; Alexe, M.; Thomas, P. A. A photoferroelectric material is more than the sum of its parts. *Nat. Mater.* **2012**, *11*, 260.
- (27) Rubio-Marcos, F.; Del Campo, A.; Marchet, P.; Fernández, J. F. Ferroelectric domain wall motion induced by polarized light. *Nat. Commun.* **2015**, *6*, 6594.
- (28) Li, T.; Lipatov, A.; Lu, H.; Lee, H.; Lee, J.-W.; Torun, E.; Wirtz, L.; Eom, C.-B.; Iñiguez, J.; Sinititskii, A.; Gruverman, A. Optical control of polarization in ferroelectric heterostructures. *Nat. Commun.* **2018**, *9*, 3344.
- (29) Liou, Y.-D.; Chiu, Y.-Y.; Hart, R. T.; Kuo, C.-Y.; Huang, Y.-L.; Wu, Y.-C.; Chopdekar, R. V.; Liu, H.-J.; Tanaka, A.; Chen, C.-T.; Chang, C.-F.; Tjeng, L. H.; Cao, Y.; Nagarajan, V.; Chu, Y.-H.; Chen, Y.-C.; Yang, J.-C. Deterministic optical control of room temperature multiferroicity in BiFeO_3 thin films. *Nat. Mater.* **2019**, *18*, 580–587.
- (30) Rubio-Marcos, F.; Ochoa, D. A.; Del Campo, A.; García, M. A.; Castro, G. R.; Fernández, J. F.; García, J. E. Reversible optical control of macroscopic polarization in ferroelectrics. *Nat. Photonics* **2018**, *12*, 29–32.
- (31) Yang, M.-M.; Alexe, M. Light-Induced Reversible Control of Ferroelectric Polarization in BiFeO_3 . *Adv. Mater.* **2018**, *30*, 1704908.
- (32) Nova, T.; Disa, A.; Fechner, M.; Cavalleri, A. Metastable ferroelectricity in optically strained SrTiO_3 . *Science* **2019**, *364*, 1075–1079.
- (33) Hadjoudis, E.; Mavridis, I. M. Photochromism and thermochromism of Schiff bases in the solid state: structural aspects. *Chem. Soc. Rev.* **2004**, *33*, 579–588.
- (34) Kobatake, S.; Takami, S.; Muto, H.; Ishikawa, T.; Irie, M. Rapid and reversible shape changes of molecular crystals on photoirradiation. *Nature* **2007**, *446*, 778–781.
- (35) Sato, O. Dynamic molecular crystals with switchable physical properties. *Nat. Chem.* **2016**, *8*, 644–656.
- (36) Saltiel, J.; Sun, Y. *Photochromism, molecules and systems*; Elsevier: 1990; p 64.
- (37) Zhao, L.; Meng, Y.-S.; Liu, Q.; Sato, O.; Shi, Q.; Oshio, H.; Liu, T. Switching the magnetic hysteresis of an $[\text{Feii}-\text{NC}-\text{Wv}]$ -based coordination polymer by photoinduced reversible spin crossover. *Nat. Chem.* **2021**, *13*, 698–704.
- (38) Irie, M.; Fukaminato, T.; Matsuda, K.; Kobatake, S. Photochromism of diarylethene molecules and crystals: memories, switches, and actuators. *Chem. Rev.* **2014**, *114*, 12174–12277.
- (39) Russew, M.-M.; Hecht, S. Photoswitches: From Molecules to Materials. *Adv. Mater.* **2010**, *22*, 3348–3360.
- (40) Sun, C.; Wade, M. T.; Lee, Y.; Orcutt, J. S.; Alloatti, L.; Georgas, M. S.; Waterman, A. S.; Shainline, J. M.; Avizienis, R. R.; Lin, S.; Moss, B. R.; Kumar, R.; Pavanello, F.; Atabaki, A. H.; Cook, H. M.; Ou, A. J.; Leu, J. C.; Chen, Y.-H.; Asanović, K.; Ram, R. J.; Popović, M. A.; Stojanović, V. M. Single-chip microprocessor that communicates directly using light. *Nature* **2015**, *528*, 534–538.
- (41) Roy, K.; Jaiswal, A.; Panda, P. Towards spike-based machine intelligence with neuromorphic computing. *Nature* **2019**, *575*, 607–617.
- (42) Uddin Ahmad, J.; Nieger, M.; Sundberg, M. R.; Leskelä, M.; Repo, T. Solid and solution structures of bulky tert-butyl substituted salicylaldehydes. *J. Mol. Struct.* **2011**, *995*, 9–19.
- (43) Kobatake, S.; Yamada, T.; Uchida, K.; Kato, N.; Irie, M. Photochromism of 1,2-Bis(2,5-dimethyl-3-thienyl)perfluoro-cyclopentene in a Single Crystalline Phase. *J. Am. Chem. Soc.* **1999**, *121*, 2380–2386.
- (44) Lee, W.-W. W.; Gan, L.-M.; Loh, T.-P. Synthesis and Photochromic Properties of Cycloalkylidene Fulgides. *Synlett* **2005**, *16*, 2473–2477.
- (45) Hu, L.; Dalgleish, S.; Matsushita, M. M.; Yoshikawa, H.; Awaga, K. Storage of an electric field for photocurrent generation in ferroelectric-functionalized organic devices. *Nat. Commun.* **2014**, *5*, 3279.
- (46) Chen, X.-G.; Song, X.-J.; Zhang, Z.-X.; Zhang, H.-Y.; Pan, Q.; Yao, J.; You, Y.-M.; Xiong, R.-G. Confinement-Driven Ferroelectricity in a Two-Dimensional Hybrid Lead Iodide Perovskite. *J. Am. Chem. Soc.* **2020**, *142*, 10212–10218.

(47) Zhang, H.-Y.; Song, X.-J.; Cheng, H.; Zeng, Y.-L.; Zhang, Y.; Li, P.-F.; Liao, W.-Q.; Xiong, R.-G. A Three-Dimensional Lead Halide Perovskite-Related Ferroelectric. *J. Am. Chem. Soc.* **2020**, *142*, 4604–4608.

(48) Zhang, W.; Xiong, R. G. Ferroelectric metal-organic frameworks. *Chem. Rev.* **2012**, *112*, 1163–1195.

(49) Zhang, H.-Y.; Chen, X.-G.; Tang, Y.-Y.; Liao, W.-Q.; Di, F.-F.; Mu, X.; Peng, H.; Xiong, R.-G. PFM (piezoresponse force microscopy)-aided design for molecular ferroelectrics. *Chem. Soc. Rev.* **2021**, *50*, 8248.

(50) Gruverman, A.; Alexe, M.; Meier, D. Piezoresponse force microscopy and nanoferroic phenomena. *Nat. Commun.* **2019**, *10*, 1661.

(51) Lee, D.; Lu, H.; Gu, Y.; Choi, S.-Y.; Li, S.-D.; Ryu, S.; Paudel, T. R.; Song, K.; Mikheev, E.; Lee, S.; Stemmer, S.; Tenne, D. A.; Oh, S. H.; Tsybal, E. Y.; Wu, X.; Chen, L.-Q.; Gruverman, A.; Eom, C. B. Emergence of room-temperature ferroelectricity at reduced dimensions. *Science* **2015**, *349*, 1314–1317.

(52) Akutagawa, T.; Koshinaka, H.; Sato, D.; Takeda, S.; Noro, S.; Takahashi, H.; Kumai, R.; Tokura, Y.; Nakamura, T. Ferroelectricity and polarity control in solid-state flip-flop supramolecular rotators. *Nat. Mater.* **2009**, *8*, 342–347.

(53) Harada, J.; Uekusa, H.; Ohashi, Y. X-ray Analysis of Structural Changes in Photochromic Salicylideneaniline Crystals. Solid-State Reaction Induced by Two-Photon Excitation. *J. Am. Chem. Soc.* **1999**, *121*, 5809–5810.

(54) Ogawa, K.; Kasahara, Y.; Ohtani, Y.; Harada, J. Crystal Structure Change for the Thermochromy of N-Salicylideneanilines. The First Observation by X-ray Diffraction. *J. Am. Chem. Soc.* **1998**, *120*, 7107–7108.

(55) Harada, J.; Ogawa, K. Pedal motion in crystals. *Chem. Soc. Rev.* **2009**, *38*, 2244–2252.